Insights Into Polarimetric Processing for Wetlands From Backscatter Modeling and Multi-Incidence Radarsat-2 Data

Frank Ahern, Brian Brisco, Kevin Murnaghan, Philip Lancaster, and Donald K. Atwood, *Member, IEEE*

***Abstract*—We have observed unexpected results using the Freeman–Durden (FD) and other polarimetric decompositions in Radarsat-2 quad-pol data from many swamps in Eastern Ontario. In particular, the decompositions reported minimal backscatter from the double-bounce mechanism in a situation where there was compelling evidence that double-bounce backscatter contributed substantially to the return. This led to a hypothesis that the FD and similar models give erroneous results because of the physics of Fresnel reflection of wood, a lossy dielectric material, that makes up the vertical reflecting surfaces in swamps. We found some support for this hypothesis in the literature, and now report on an extensive theoretical and observational investigation. This work has shown that the Freeman-Durden decomposition, and other decompositions that use the same logic, will often mistake double-bounce backscatter as single-bounce backscatter in wetlands. This is a consequence of the fundamental physics of Fresnel reflection. It is important for users to be aware of this pitfall. Double-bounce backscatter from natural surfaces can be identified without recourse to polarimetric decomposition. The simplest, and most reliable, indicator of double-bounce backscatter is a high return in HH polarization. Double-bounce backscatter will generally produce higher return in HH than any other scattering mechanism. If both HH and VV polarizations are available, a high HH/VV intensity ratio is also a strong indicator of double-bounce backscatter. Additional modeling efforts are expected to provide further insights that can lead to improved applications of polarimetric data.**

***Index Terms*—C-band, decomposition, Fresnel reflection, polarimetry, SAR.**

Manuscript received December 16, 2017; revised March 8, 2018 and May 13, 2018; accepted June 13, 2018. Date of publication July 22, 2018; date of current version September 5, 2018. The work of F. Ahern, B. Brisco, and K. Murnaghan was supported in part by the Remote Sensing Science program at the Canada Centre for Remote Sensing and in part by the Public Safety Floodplain Characterization Project at the Canada Centre for Mapping and Earth Observation. The work of P. Lancaster was supported by TerreVista Earth Imaging. The work of D. K. Atwood was supported by the Michigan Tech Research Institute. *(Corresponding author: Frank Ahern.)*

F. Ahern is with the TerreVista Earth Imaging, Brockville, ON K6V 1A3, Canada (e-mail: NGC5128@bell.net).

B. Brisco and K. Murnaghan are with the Canada Centre for Mapping and Earth Observation, Natural Resources Canada, Ottawa, ON K1A 0Y7, Canada (e-mail: brian.brisco@canada.ca; kevin.murnaghan@canada.ca).

P. Lancaster is with the Lancaster Geographics, Eganville, ON K0J 1T0, Canada (e-mail: Philips.Lancaster@gmail.com).

D. K. Atwood is retired from the Michigan Tech Research Institute, Ann Arbor, MI 48105-1579 USA (e-mail: atwooddk@gmail.com).

Color versions of one or more of the figures in this paper are available online at http://ieeexplore.ieee.org.

Digital Object Identifier 10.1109/JSTARS.2018.2850155

I. Introduction

In 2010, the Canada Centre for Remote Sensing initiated a program to investigate and develop the use of interferometric and polarimetric data from Radarsat-2 for inland surface water applications. These include detection of short-term flooding, where floodwater inundates vegetation that is normally not flooded, detection of permanent or near-permanent water under herbaceous and woody vegetation to identify marshes and swamps, respectively, characterization of plant communities in swamps and marshes, and detection of changes in swamps and marshes. A test site was established in the Upper Ottawa Valley, approximately 160 km west of Ottawa, where wetlands are abundant. One author (Ahern) resided in this area and could readily provide *in situ* observations. Interferometric observations using the Spotlight mode indicated a strong contribution of coherent backscatter in many wetlands. Specifically, individual HH images showed strong backscatter from inundated areas with emergent vegetation. Interferometric pairs showed high coherence in inundated areas. Changes in water level could readily be observed as phase changes, indicating a dominant double bounce scattering mechanism [1]. In 2011, we acquired RADARSAT-2 polarimetric data for ten swamps at an incidence angle of 22°. Several different polarimetric decompositions attributed a very small fraction of the backscatter from these swamps to the double-bounce mechanism [2]. These decompositions all use the phase difference between the HH and VV backscatter (co-pol phase difference, or CPD) as the criterion for distinguishing single bounce (CPD $< 90°$) from double bounce (CPD $> 90°$) [3]–[6]. Since the CPD we observed in our data was predominantly less than 90°, we attributed the anomalous decomposition results to the small CPD values we observed. In the course of our investigation, we also found several papers that suggested that these low values of CPD might be a consequence of the physics of microwave reflection by water and vegetation [7]–[10]. Thirion-Lefevre and Guinvarc'h [10] introduce the terminology "Double Brewster Effect" and show that this effect can result in a high ratio of HH to VV backscatter over a large range of incidence angles.

The physics of the backscattering process in swamps such as those in this study can be modeled as the coherent sum of electromagnetic waves scattered by cylinders above a ground plane that can be tilted relative to horizontal [11]. This paper has been extended [12] to allow for a range of trunk lengths and

inclinations relative to vertical, and for variable surface roughness. For the case of monostatic backscatter, these two references show enhanced HH/VV backscatter ratios when the geometrical conditions for double-bounce backscatter are present.

Observations of rice plants with a water substrate [13]–[15] show high values of the HH/VV backscatter ratios and the CPD that are similar to those of trees in water that we discuss in Sections IV-G and IV-H.

In this modeling, the magnitude and phase of the scattered waves, typically described using complex numbers, are governed by the index of refraction, which is the square-root of the complex dielectric constant (or permittivity). The angular distribution (antenna pattern) of the backscattered radiation is calculated as the coherent sum of the waves scattered by the individual scatterers. In short, the radar backscatter of a target consisting of vegetation over a dielectric ground plane is governed by the dielectric properties of the plane, the dielectric properties of the scatterers, and the number, size, shape, and geometric orientation of the scatters. It is apparent that implementing a realistic and accurate backscattering model for a swamp forest can be a daunting task. In this paper, we describe insights we have gained by using a simple dihedral model of polarimetric backscatter in conjunction with a large suite of fully polarimetric observations of simple swamps with RADARSAT-2 data. Further progress will require a more realistic model.

II. Theoretical Considerations and Calculations

A. Surface Reflection

When electromagnetic radiation encounters a surface such as soil or water where there is an abrupt change in the index of refraction (discussed in Section II-B), a fraction of the radiation is reflected, while the remainder enters the substrate material and is usually absorbed and converted to heat energy. In the simplest case, the surface is smooth compared to the wavelength. There are various criteria for smoothness, ranging from variations in the height of the reflecting surface of $\lambda/4$ to as small as $\lambda/20$. Scatter from a smooth planar surface is called specular (mirror) reflection and is defined by the Fresnel reflection equations (see Section II-B). All of the radiation will be forward-scattered, with the angle of reflection equal to the angle of incidence. When the planar surface is not smooth compared to the wavelength, the scattering is called diffuse scattering, and the radiation is spread out into a beam centered in the specular direction, with the beamwidth proportional to the roughness of the surface. Diffuse surface scattering is illustrated in many texts (e.g., [16, p. 129]; [17, p. 139]).

It is apparent, then, that smooth or slightly rough planar surfaces will produce zero or little backscatter. However, if a vertical surface is present in addition to a horizontal surface, the forward scatter from one surface will also be forward scattered from the second surface, and these two scattering events will result in backscatter in the general direction of the source of illumination. If the line of intersection of the two planes is oriented perpendicular to the radar illumination direction, the backscatter will be directed toward the source of illumination. This configuration is called a dihedral corner reflector, and is well-illustrated in [16, pp. 54, 124] and [17, p. 102].

B. Fresnel Equations

Electromagnetic radiation is described as a transverse electromagnetic wave according to Maxwell's equations. When such a wave encounters a plane where the index of refraction changes, it is reflected and refracted, as described by the Fresnel equations [16]–[20]. It is conventional to use the term "reflection coefficient" to refer to the ratio of the received to transmitted electric field strength, and the term "reflectivity" to refer to the ratio of the received to transmitted power, which is the square of the modulus of the field strength. The corresponding concepts in monostatic radar remote sensing are the elements of the scattering matrix [17], and the backscattered power, which is the square modulus of the scattering matrix elements.

The only free parameters in the Fresnel equations are the indices of refraction, n_0 and n_1, of the incident and reflecting media. These are complex numbers, related to the intrinsic electrical and magnetic properties of the media through

$$n_i = \sqrt{\varepsilon_r \mu_r} \tag{1}$$

where ε_r is the material's relative (electrical) permittivity, also frequently called the dielectric constant, and μ_r is the material's relative (magnetic) permittivity, equal to 1 for nonmagnetic materials.

C. Fresnel Reflection From Single Planes of Glass, Water, and Wood; the Brewster Angle

The reflection of optical radiation by glass provides a starting point that is covered in varying levels of detail in well-known optics and electrodynamics texts [18]–[20].

In Fig. 1, we illustrate the HH and VV reflectivity and the HH-VV phase difference (CPD) for a single reflection from planar surfaces of materials of interest. We begin with a glass at optical frequencies with an index of refraction of $1.5 + 0.05i$. This provides a comparison with a frequently illustrated case. Note that this geometry would correspond to a bistatic radar, with the angle of reflection equal to the angle of incidence. The reflectivity, *R*, is the ratio of the reflected power to the incident power, and is illustrated as a function of the incidence angle, where 0° corresponds to normal incidence. Note that the HH and VV reflectivities are equal (about 4%) at 0° as one would expect. However, while the HH reflectivity increases monotonically as the angle of incidence increases, approaching 100% at grazing incidence, the VV reflectivity decreases to a minimum close to 0 at an incidence angle near 56°, and then increases rapidly, approaching 100% at grazing incidence. Note also that for VV radiation, the CPD makes a sudden transition from near 180° to near 0°, also at an incidence angle near 56°. The angle where the VV reflectivity reaches a minimum and the phase transition is most rapid is called the Brewster angle. These phenomena are characteristic of reflection from dielectric (nonconducting) materials. When electromagnetic radiation is reflected from conducting materials such as metals, the HH and VV reflectivities are very close to 100%, while the Brewster-angle effect moves

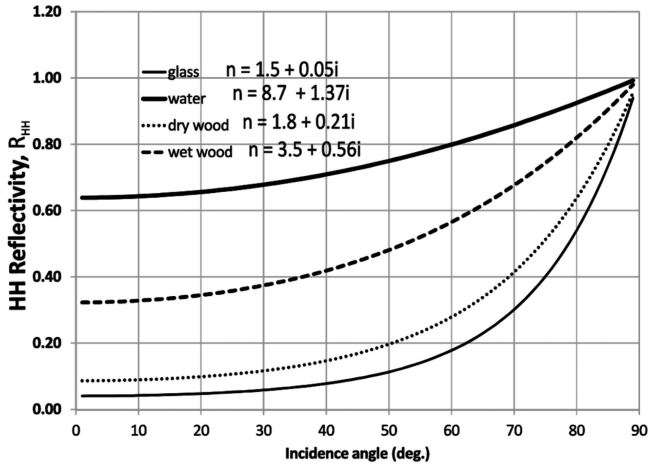

(a)

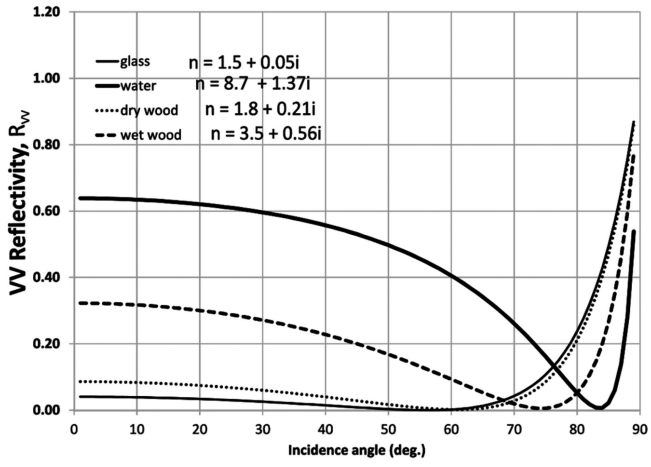

(b)

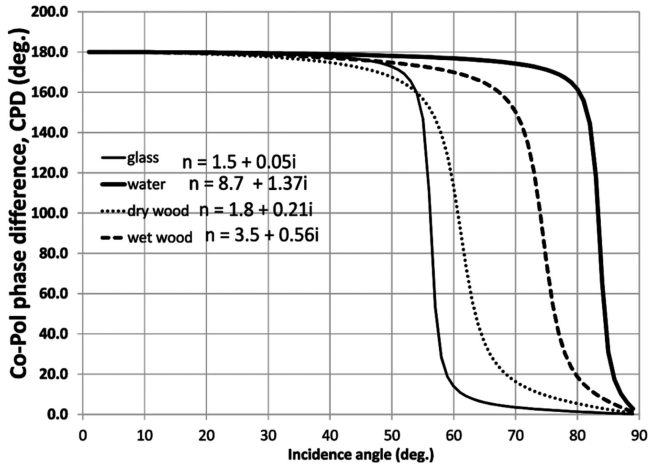

(c)

Fig. 1. Reflectivity and CPD values for glass, water, dry wood, and wet wood, plotted as a function of incidence angle. (a) Reflectivity for HH geometry. (b) Reflectivity for VV geometry. (c) CPD.

to near-grazing incidence and becomes nearly impossible to observe.

Ulaby and El-Rayes [21] present mathematical models to calculate the dielectric constants of water and vegetation that have been widely used by the remote sensing community. We have used their equations (2) and (10) to calculate the dielectric constants of fresh water and vegetation for the RADARSAT-2 frequency of 5.4 GHz, followed by (1) to calculate the corresponding indices of refraction. The indices of refraction used to produce the curves in Fig. 1 are 8.737 + 1.374i for water, 1.7974 + 0.206i for dry wood, and 3.5311 + 0.5637i for wet wood. Dry wood and wet wood are calculated on the basis of their gravimetric moisture, Mg. For these examples, Mg (dry) = 0.175, and Mg (wet) = 0.45, based on extensive measurements made with Black Ash (*Fraxinus nigra*) and Eastern White Cedar (*Thuja occidentalis*) during the summer of 2016. The dry value corresponds to dry wood typical of trees in a swamp that have been dead for many years, and the wet value corresponds to wood that is saturated with water so it barely floats.

Dry wood has an index of refraction and reflectance properties at C-band that are similar to the properties of glass in the optical region. Fig. 1 shows the expected difference between HH reflectivity and VV reflectivity. While HH reflectivity increases monotonically from normal incidence (0°) to grazing incidence (approaching 90°), VV reflectivity decreases to a value near zero at the Brewster angle, and then rises rapidly to approach the HH reflectivity near grazing incidence. Water, having a high index of refraction, has a Brewster angle greater than 80°. Wet wood has a Brewster angle between that of dry wood and water, as expected.

D. Dihedral Model

In our quest to improve our understanding of backscatter physics from swamps and other wetlands, it has proven very informative to make a simple model for dihedrals using the Fresnel equations as described above. In its simplest form, our model considers the reflection of a monostatic radar signal from two plane surfaces, one horizontal, and the other vertical, oriented with the line of intersection orthogonal to the radar beam.

Our model calculates scattering matrix elements S_{ij} for a dihedral. The scattering matrix is also known as the Sinclair matrix. As shown by [17, eq. 3.40, p. 82], the scattering matrix elements can be defined using the equation

$$\begin{bmatrix} E^b_{\mathrm{H}} \\ E^b_{\mathrm{V}} \end{bmatrix} = \begin{bmatrix} S_{\mathrm{HH}} & S_{\mathrm{HV}} \\ S_{\mathrm{VH}} & S_{\mathrm{VV}} \end{bmatrix} \begin{bmatrix} E^i_{\mathrm{H}} \\ E^i_{\mathrm{V}} \end{bmatrix} \tag{2}$$

where E represents the complex electric field, the superscripts i and b represent incident and backscatter radiation, and subscripts H and V represent the H and V polarizations. Note that algebraically, and thus physically, these elements correspond to ratios of the backscattered to incident fields. For the simple case of a dihedral with its vertex orthogonal to the illumination from a monostatic radar

$$\begin{aligned} S_{\mathrm{HH}} &= C\left[\mathrm{FH_H}\left(\theta\right) + \mathrm{FV_H}\left(90-\theta\right)\right] \\ S_{\mathrm{VV}} &= C\left[\mathrm{FH_V}\left(\theta\right) + \mathrm{FV_V}\left(90-\theta\right)\right] \\ S_{\mathrm{HV}} &= S_{\mathrm{VH}} = 0 \end{aligned} \tag{3}$$

where $\mathrm{FH_H}$ and $\mathrm{FV_H}$ are the Fresnel reflection coefficients for horizontal polarization reflecting from the horizontal and

vertical planes, FH_V and FV_V are the Fresnel reflection coefficients for vertical polarization reflecting from the horizontal and vertical planes, θ is the radar incidence angle, and C is a calibration constant.

Three fundamental variables are calculated from these scattering matrix elements: The reflectivities $R_{HH} = |S_{HH}|^2$, $R_{VV} = |S_{VV}|^2$, and the co-pol phase difference, CPD $= \text{Arg}(S_{HH}S_{VV}^*)$.

Having looked at the physics of single surfaces in Section II-C, we now examine the characteristics of relevant combinations of different materials in the form of a dihedral. The insights gained from this exercise will apply to smooth surfaces, but we must keep in mind that the physics will change when the surfaces become rough [16 p. 125ff].

The only free parameters in our model are the complex indices of refraction for air, and for each of the two media making up our reflecting planes. The index of refraction of air is taken to be $n_0 = 1.0 + 0.0$i, while n_1 is the index of refraction of the (horizontal) ground plane, and n_2 is the index of refraction of the vertical plane. The values used were those described in the discussion of reflection from single planes.

E. Insights from Modeling

Fig. 2 shows how three fundamental parameters vary as a function of radar incidence angle: the reflectivity (ratio of reflected to incident power) for HH radiation (R_{HH}), the reflectivity for VV radiation (R_{VV}), and the CPD. These figures have curves for four examples: a metal-metal dihedral, a metal-wood dihedral for dry wood, and two water–wood dihedrals, with dry and wet wood.

1) Metal Dihedrals: The backscattering behaviour of metal dihedrals is a simple and well-understood case. The reflectivities for both the HH and VV radiation are nearly 100% across the range of incidence angles [see Fig. 2(a) and (b)], while the CPD is nearly 180° across the range, as shown in Fig. 2(c).

This simple behavior of metal dihedrals in comparison to single-bounce backscatter has been used by a number of polarimetric decomposition models to distinguish between double-bounce and single-bounce backscatter [3]–[6], as reviewed in [2]. However, the backscatter from lossy dielectric materials behaves differently. In particular, because of the Brewster angle effect, there is a transition in CPD from near 0° to near 180° that can cause these decomposition models to indicate single-bounce backscatter when double-bounce backscatter is clearly dominant [2].

2) Metal-Dry Wood: In the case of a vertical plane of wood on a horizontal metal substrate, we see the same curves for dry wood that we saw for Fresnel reflection in Fig. 1(a)–(c), but with the incidence angle scale reversed. In other words, the incidence angle of the microwaves on the wooden plane is the complement of the radar incidence angle, because of the geometry of the dihedral reflection. The HH and VV reflectivity values are high at steep incidence angles and drop off as the incidence angle increases. The CPD is low at steep incidence and transitions to near –180° at the complement of the Brewster angle for single-plane Fresnel reflection.

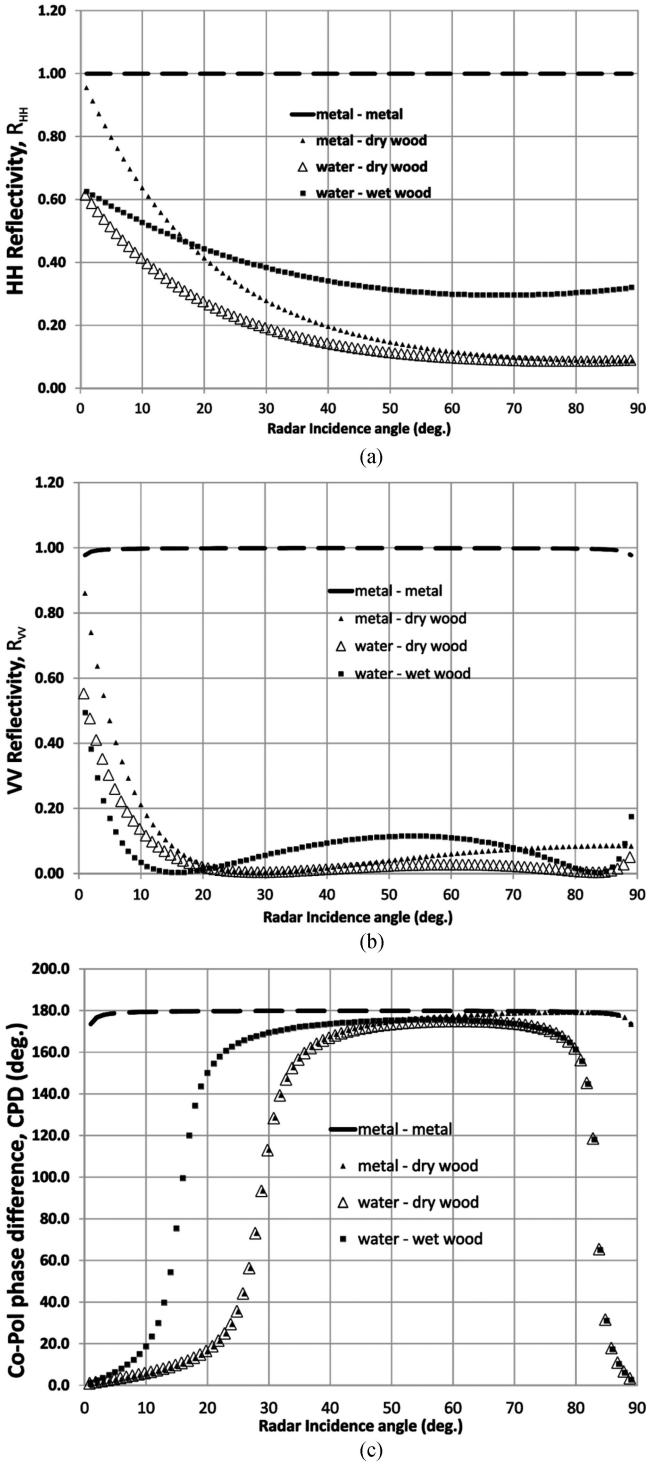

Fig. 2. Reflectivity and CPD values for metal-metal, metal-dry wood, water-dry wood, and water-wet wood dihedrals. (a) Reflectivity for HH geometry. (b) Reflectivity for VV geometry. (c) CPD.

3) Water-Dry Wood: When fresh water is substituted for metal as the substrate, there are two incidence angles where the Brewster angle effect is seen for the VV orientation. The dry wood shows the same behavior in R_{VV} reflectivity and CPD near 30° incidence as with a metal substrate, but in addition, we also see Brewster angle effects that result from the dielectric

constant of water at an incidence angle near 85°. These effects occur outside the range of incidence angle typically used for space-borne radars, but we note them in our model results.

4) Water-Wet Wood: When the gravimetric moisture of wood is increased from $M_g = 0.175$ (very dry), to $M_g = 0.45$ (very wet), the HH reflectivity of the dihedral increases, doubling at incidence angles greater than 25°, while the VV reflectivity decreases, approaching zero near the Brewster angle, and the Brewster transition in CPD shifts from about 28° down to about 16°. These are large changes, pointing toward potential applications. Of course real-world conditions can be much more complicated than our simple dihedral model, and operational applications may be much more difficult to achieve, as researchers have found when trying to estimate soil moisture from space. Nonetheless, we are encouraged to continue our modeling efforts to explore possible applications suggested by these results.

III. Observations and Data Processing

In 2016, we obtained a total of 43 RADARSAT-2 data acquisitions over the Lake Clear study area, centered at 77.2703 West longitude and 45.4527 North latitude. We have been investigating interferometric and polarimetric C-band data for inland water applications at that study area since 2010 [1], [2]. The acquisitions discussed here were obtained from May 1 to October 30, at incidence angles ranging from 22° to 49°. Table I shows the details of each acquisition, while Fig. 3 shows that our acquisitions are well distributed in incidence angle throughout the time frame, and include both descending (∼06:00 local standard time) and ascending (∼18:00 local standard time) passes. This dataset will enable us to examine the effects of incidence angle. Note that the illumination azimuth angle will differ by approximately 160° between ascending and descending overpasses. However, high-resolution optical imaging shows the Corrigan swamp investigated here is uniform in azimuth. Acquisition of both ascending and descending passes provides a greater variety of moisture conditions because dew can occur in the morning, but not in the afternoon.

TABLE I
RADARSAT-2 Data Acquisitions for 2016 at Lake Clear Study Site

		Day in			Asc or	Resolution (m)		Observed
Month	Day	2016	Beam	Inc	Des	Az	Gnd Rng	Moisture
5	01	122	FQ8	27.8	D	5.1	11.2	dry
5	04	125	FQ14	34.3	A	5.1	9.3	dry
5	14	135	FQ23	42.6	A	5.1	7.7	damp
5	18	139	FQ4	23.1	A	5.1	13.3	damp
5	18	139	FQ3	21.9	D	5.1	14.0	dry
5	25	146	FQ8	27.8	D	5.1	11.2	damp
6	11	163	FQ4	23.1	A	5.1	13.3	wet
6	11	163	FQ3	21.9	D	5.1	14.0	damp
6	14	166	FQ18	38.2	A	5.1	8.5	dry
6	25	177	FQ12	32.2	D	5.1	9.8	dry
6	28	180	FQ9	28.9	A	5.1	10.8	dry
6	29	181	FQ31	48.9	D	5.1	6.9	dry
7	05	187	FQ4	23.1	A	5.1	13.3	dry
7	08	190	FQ18	38.2	A	5.1	8.5	wet
7	09	191	FQ22	41.7	D	5.1	7.8	wet
7	12	194	FQ8	27.8	D	5.1	11.2	dry
7	15	197	FQ14	34.3	A	5.1	9.3	wet
7	16	198	FQ26	45.1	D	5.1	7.4	wet
7	19	201	FQ12	32.2	D	5.1	9.8	damp
7	22	204	FQ9	28.9	A	5.1	10.8	dry
7	25	207	FQ23	42.6	A	5.1	7.7	dry
7	26	208	FQ17	37.2	D	5.1	8.7	dry
7	29	211	FQ4	23.1	A	5.1	13.3	damp
7	29	211	FQ3	21.9	D	5.1	14.0	dry
8	25	238	FQ18	38.2	A	5.1	8.5	dry
8	26	239	FQ22	41.7	D	5.1	7.8	damp
8	29	242	FQ8	27.8	D	5.1	11.2	damp
9	01	245	FQ14	34.3	A	5.1	9.3	wet
9	05	249	FQ12	32.2	D	5.1	9.8	damp
9	08	252	FQ9	28.9	A	5.1	10.8	dry
9	11	255	FQ23	42.6	A	5.1	7.7	dry
9	15	259	FQ4	23.1	A	5.1	13.3	wet
9	15	259	FQ3	21.9	D	5.1	14.0	dry
9	22	266	FQ8	27.8	D	5.1	11.2	damp
9	25	269	FQ14	34.3	A	5.1	9.3	damp
9	29	273	FQ12	32.2	D	5.1	9.8	dry
10	03	277	FQ31	48.9	D	5.1	6.9	wet
10	05	279	FQ23	42.6	A	5.1	7.7	dry
10	09	283	FQ4	23.1	A	5.1	13.3	damp
10	09	283	FQ3	21.9	D	5.1	14.0	dry
10	27	301	FQ31	48.9	D	5.1	6.9	dry
10	29	303	FQ23	42.6	A	5.1	7.7	wet
10	30	304	FQ17	37.2	D	5.1	8.7	damp

A. Characteristics of the Corrigan Swamp

For this initial work, we have concentrated on data from the Corrigan Swamp, a large (92 ha) area of standing water densely populated with numerous dead black ash and speckled alder (*Alnus incana*) trees. In February of 2014, we sampled the tree population taking advantage of the solid ice cover to provide access to the trees. Fig. 4 shows a typical view of the Corrigan Swamp in winter. Note the large number of small diameter trees, and the small number of large diameter trees. Note also the relatively small number of upper branches, most of which are short and small. This is the typical form of black ash found in swamps. In this case, and many other cases in southern Canadian wetlands, the trees are all dead. Black ash, as well as eastern white cedar (*Thuja occidentalis*) and tamarack (*Larix laricina*) frequently grow as monocultures in wet areas. Flooding, through human activities or beaver damming, will kill these stands, which then persist for decades as dead tree swamps.

The summary characteristics of the tree population of the Corrigan swamp are as follows:

1) average stem density: 1.04 stems/m^2;
2) average canopy height: 5.8 m;
3) stem diameter (breast height, 1.6 m above ice surface): 69% of stems were 3 cm or less in diameter, and 96% of the stems were 10 cm or less in diameter. The mean value is not meaningful because the distribution is highly skewed toward small diameters.

B. Radarsat Data Analysis

Image tiles in single-look-complex (SLC) format were ingested and converted to elements C_{11}, C_{22}, C_{33}, and C_{13} of

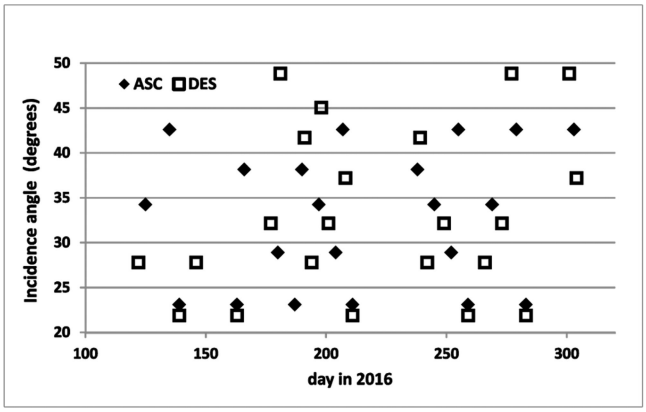

Fig. 3. Radarsat-2 data acquisitions for Lake Clear study area, 2016. ASC = ascending orbit (PM overpass); DES = descending orbit (AM overpass).

Fig. 4. View of the Corrigan swamp during winter fieldwork showing the characteristics of the trees including the presence of upper branches and nonvertical trunks that can cause cross-polarized backscatter.

the 3×3 covariance matrix [17, p. 20] commonly referred to as $C3$:

$$C3 = \begin{bmatrix} \left\langle |S_{\mathrm{HH}}|^2 \right\rangle & \sqrt{2}\,\langle S_{\mathrm{HH}} S_{\mathrm{HV}}^* \rangle & \langle S_{\mathrm{HH}} S_{\mathrm{VV}}^* \rangle \\ \sqrt{2}\,\langle S_{\mathrm{HV}} S_{\mathrm{HH}}^* \rangle & 2\left\langle |S_{\mathrm{HV}}|^2 \right\rangle & \sqrt{2}\,\langle S_{\mathrm{HV}} S_{\mathrm{VV}}^* \rangle \\ \langle S_{\mathrm{VV}} S_{\mathrm{HH}}^* \rangle & \sqrt{2}\,\langle S_{\mathrm{VV}} S_{\mathrm{HV}}^* \rangle & \left\langle |S_{\mathrm{VV}}|^2 \right\rangle \end{bmatrix}. \quad (4)$$

The S_{ij} are the scattering matrix elements for the four polarization combinations, provided as four bands of complex numbers in the SLC data. These are dimensionless complex numbers proportional to the ratio of backscattered to incident power. Note that this formulation assumes symmetry: $S_{\mathrm{HV}} = S_{\mathrm{VH}}$, which is expected for a monostatic radar when Faraday rotation is negligible [17]. The features we will examine in this paper are the diagonal elements of $C3$. These are the expectation values (means) of the square magnitudes of the like-pol (S_{HH} and S_{VV}) and cross-pol (S_{HV}) scattering coefficients. In keeping with customary terminology, we will refer to these features as backscattering coefficients.

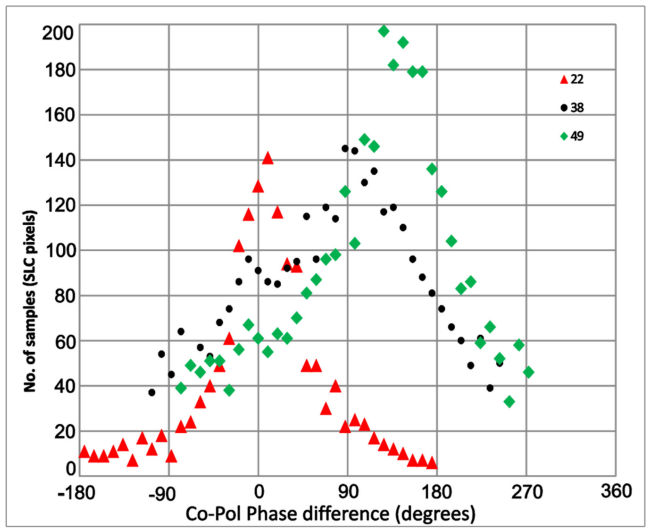

Fig. 5. Histograms of CPD. Three curves are shown, for steep (22°), intermediate (38°), and shallow (49°) incidence angles.

The complex S_{HH} image pixels are converted to a real image by taking the square of the magnitude. This HH image typically produces a strong return from swamps with dead trees [2], [22], [23]. It was used to delineate the boundary of the Corrigan Swamp visually, to produce a polygon mask to enable extraction of the desired data from selected $C3$ elements.

Because of the excellent RADARSAT-2 repeat-pass geometry, it proved possible and desirable to add all of the HH images for each individual incidence angle. This produced a superior image to delineate the polygon mask for the Corrigan Swamp at that incidence angle by reducing speckle. Note that no geometric correction was performed: the polygon masks were made using, and applied to, the SLC images.

Once the polygon masks were available, they were used to extract mean values for the real numbers C_{11}, C_{22}, and C_{33}. The mean value corresponds to the expectation value indicated by the angle brackets in (4). A histogram of individual $S_{\mathrm{HV}} S_{\mathrm{VV}}^*$ phase angles for all of the masked pixels was calculated to inspect for asymmetries and other anomalies. Our dataset was free of anomalies, and the mean CPD for the Corrigan Swamp area was calculated from the histogram values.

Three histograms are shown in Fig. 5. These indicate the distribution of CPD values for representative single dates at incidence angles of 22° (steep), 38° (intermediate), and 49° (shallow). The vertical axis represents counts in each of 37 bins of width 9.73° each. The 37 bins span a 360° range. The red triangles labeled 22 are produced from data acquired on May 18, 2016 at an incidence angle of 22°. Note that the histogram is centered near 0° and is narrow and symmetric. The histogram labeled 38 (black dots) is produced from data acquired on June 14, 2016 at an incidence angle of 38°. Now the peak is shifted to values near 90°. Finally, the histogram labeled 49 (green diamonds) is produced from data acquired on October 27, 2016 at an incidence angle of 49°. The peak is shifted to values near 130°. This observed shift in the histogram with increasing incidence angle is very similar to histograms we have observed

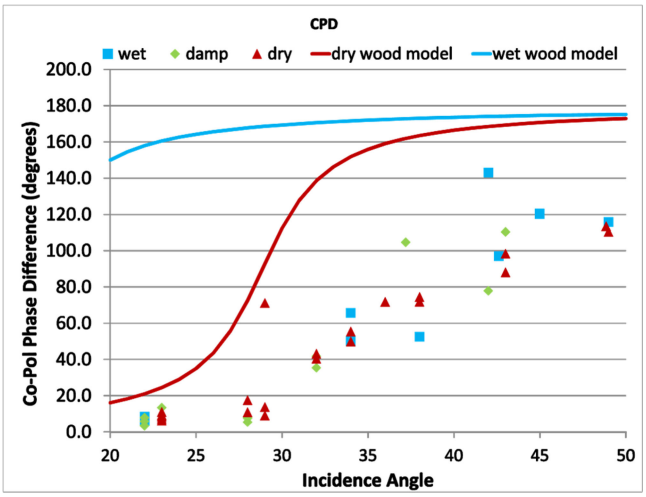

Fig. 6. Observed mean CPD (individual points) as a function of incidence angle compared to theoretical curves of a dihedral model with dry and wet wood planes emergent from a fresh water substrate.

at varying incidence angles from this and similar swamps with earlier data acquisitions [2]. We compare the mean CPD derived from the histograms for all of our observations with the predictions of the dihedral model in Section IV-A.

It is also interesting to note that these histogram curves have minimum values above zero counts. In other words, there is a "pedestal" of pixels with random phase. This pedestal is relatively small ($\sim$10 counts) for the steep incidence data, but larger ($\sim$40 counts) for the shallow incidence data.

IV. Results and Discussion

In this section, we compare a number of measured polarimetric features with theoretical curves produced using the dihedral model discussed above. We first calculated the CPD as the argument of C_{13} for the RADARSAT-2 data and as the argument of $r_{\mathrm{HH}} \cdot r^*_{\mathrm{VV}}$ for the dihedral, where r_{HH} and r_{VV} are the (complex) amplitude reflection coefficients. These two measures of CPD are physically equivalent. This feature is central to our hypothesis [2] that the physics of Fresnel reflection creates situations where double-bounce backscatter exhibits low values of CPD, which can result in incorrect results from frequently used polarimetric decompositions. The remaining polarimetric features are derived from backscatter coefficients from the covariance matrix $C3$ (4). The corresponding features from the dihedral calculations are the reflectivity values, R_{HH} and R_{VV}, which indicate the ratio of reflected to incident power. These two measures are physically equivalent, differing only by a calibration factor. These polarimetric features are important in the context of increasing our understanding of the physics, showing shortcomings of our model, and making recommendations for practical applications. Finally, we look at cross-pol features, because we observe a significant amount of cross-pol backscatter in our data even though the dihedral model predicts zero cross-pol backscatter for our monostatic geometry.

A. Co-Pol Phase Difference (See Fig. 6)

The CPD of the observed points shows a Brewster-type transition from near 10° CPD at 20° incidence to about 120° CPD above 45° incidence. Interestingly, there is no clear separation between the wet samples and the dry and damp samples. The observed change in CPD is a clear indication that the decomposition models that use CPD as a discriminant between the single-bounce and double-bounce backscatter mechanisms cannot be relied upon for swamps like those we are observing. At steep incidence angles (less than about 35°), nearly all of the pixels will have values of the CPD less than 90°, the threshold for double-bounce classification. The backscatter mechanism will thus be incorrectly classified as single-bounce backscatter in decomposition models that use the 90° threshold.

The dihedral curves in Fig. 6 [see also Fig. 2(c)] show the Brewster phase transition at steeper incidence angles than we observe with RADARSAT-2. With our dihedral model, the only way to get a better fit would be to decrease the wood moisture content to a value lower than our current dry model, which seems unlikely to be the case in a natural environment.

It is very interesting to note that [7] shows a CPD scatter diagram very similar to our observations for a case of corn fields observed at L-band. The authors of that paper fit a model of dielectric cylinders over a soil substrate to their data points. The dielectric constant that provided a good fit was $\varepsilon = 6.5–0.5\mathrm{i}$, which corresponds to an index of refraction of $2.45 – 0.102\mathrm{i}$ and a gravimetric moisture of 0.25. They also point out that the CPD is reduced at greater incidence angles by a canopy propagation effect. As they were using airborne data, they were able to observe this effect at large incidence angles. Given the success of [7] with a relatively simple model, we are encouraged to pursue that line of investigation.

B. Like-pol Backscatter, $C_{11} + C_{33}$ [See Fig. 7(a)]

The first polarimetric backscatter feature to be examined is $C_{11} + C_{33}$, the sum of the HH and VV backscatter coefficients. Fig. 7(a) displays the RADARSAT-2 observations across a range of incidence angles from 22° to 49°. The backscatter data are separated into three moisture conditions: dry, damp, and wet. These classes were assigned on the basis of the meteorological conditions in 24 h up to the overpass. Dry conditions correspond to no rain during 24 h, and no dew at the time of the overpass. The observations of other moisture conditions were made *in situ* just before the overpass. Damp conditions were assigned in the case of light rain or the presence of dew at the time of the overpass. Wet conditions were assigned when there was heavy rain during 24 h before the overpass, without drying conditions immediately prior to the overpass. This was also corroborated with *in situ* observations at the time of the overpass.

We note that the dry and damp points together produce a smooth curve that decreases with increasing incidence angle. The wet points fall together with the dry and damp points for incidence angles less than 30°, but do not fall off with incidence angle as quickly as the dry and damp points, becoming separated (in most cases) from the curve formed by the dry and damp points.

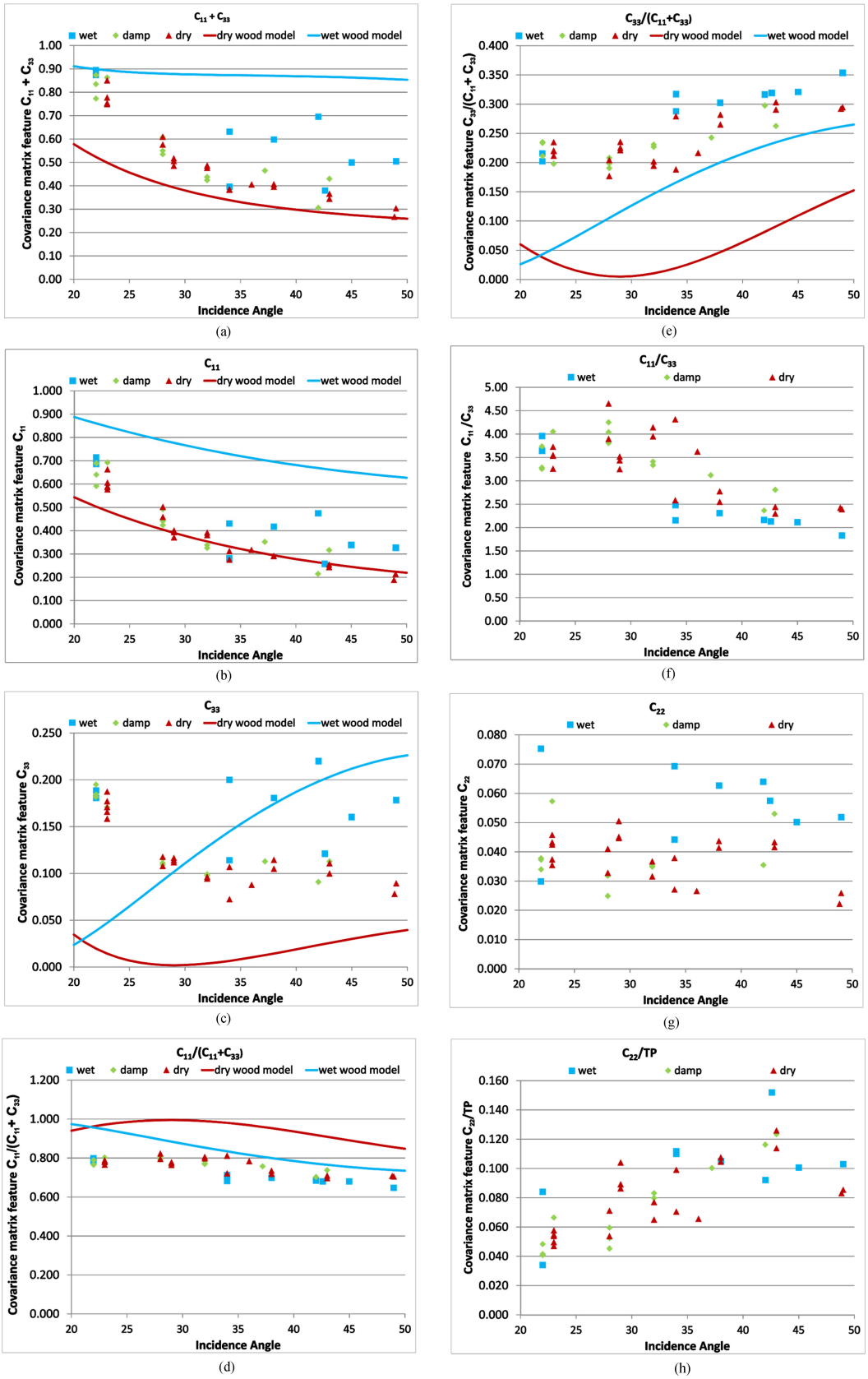

Fig. 7. (a) Like-pol backscatter $(C_{11} + C_{33})$ as a function of incidence angle. (b) HH backscatter coefficient (C_{11}) as a function of incidence angle. (c) VV backscatter coefficient (C_{33}) as a function of incidence angle. (d) Backscatter feature $C_{11}/(C_{11} + C_{33})$ as a function of incidence angle. (e) Backscatter feature $C_{33}/(C_{11} + C_{33})$ as a function of incidence angle. (f) HH/VV backscatter ratio C_{11}/C_{33} as a function of incidence angle. (g) Cross-pol backscatter $C_{33}/(C_{11} + C_{33})$ as a function of incidence angle. (h) Cross-pol ratio $C_{33}/(C_{11} + C_{22} + C_{33})$ as a function of incidence angle.

The dry and wet wood dihedral model curves were adjusted with a single multiplicative calibration factor [C in (3)] to fit the observed points. This factor, which was 2.0, was used for all of the dihedral calculations reported in this paper. We note that the dry and wet dihedral curves bracket the observed points and that the dry curve has a shape similar to the shape of the dry and damp RADARSAT-2 points. The curve for the wet wood model lies above the observed points. This is not surprising, because the dihedral model was made with the assumption of an infinitely thick layer of wood with a gravimetric moisture of $M_g = 0.45$, corresponding to fully saturated wood, while the actual penetration of water into the trees will be only a few millimetres, and the stem diameter is less than 3 cm in majority of cases.

C. HH Backscatter Coefficient, C_{11} [See Fig. 7(b)]

Since the HH backscatter is considerably larger than the VV backscatter, it is not surprising that the curve for C_{11} as a function of incidence angle is similar to that of $C_{11} + C_{33}$ [see Fig. 7(a)]. We see the same monotonic decline with increasing incidence, and curvature of the observed points similar to the curve for the dry wood dihedral. However, there is smaller separation between the wet points and the dry and damp points.

D. VV Backscatter Coefficient, C_{33} [See Fig. 7(c)]

VV is the polarization where the Fresnel reflection causes a decrease to near-zero reflectivity at the Brewster angle, as shown for the dry wood model curve in Fig. 7(c). We see that the dry and damp wood observations also exhibit a curve with a shape to that predicted with the dihedral model, but offset to a higher level of backscatter. An increase in the imaginary part of the index of refraction for wood can cause that kind of offset. That would require an increase in the ionic conductivity of the bound water in the wood. Another possibility is that some of the surface reflectivity of the wood, water, or both is caused by Bragg scattering. As pointed out by [16], with Bragg scattering, the VV component is greater than the HH component, and does not exhibit a decrease in reflectivity at the Brewster angle.

The curve for the wet wood model has a Brewster angle at an incidence angle smaller than 20°, outside the plotted range. The wet wood curve rises to a value higher than the dry wood curve and passes through the scatter of points associated with wet conditions, but the fit is not a good one. Nonetheless, the separation between the wet points and the dry and damp points is consistent with the predictions of Fresnel physics.

To summarize, the VV backscatter is greater than predicted by the dihedral model. Possible causes include slight roughening of the water surface by wind, or the presence of living plants or dead plant parts on the surface, which can also roughen it. These possibilities must be addressed in future modelling efforts.

E. $C_{11}/(C_{11} + C_{33})$ and $C_{33}/(C_{11} + C_{33})$ [See Fig. 7(d) and (e)]

The ratio $C_{11}/(C_{11} + C_{33})$ is nearly independent of incidence angle, with the RADARSAT-2 observations lying about 10% lower than the model curves [see Fig. 7(d)]. This lower ratio is a result of the increased amount of VV backscatter in the observations, which increases the denominator in the relationship.

The RADARSAT-2 observations of $C_{33}/(C_{11} + C_{33})$ show curves that are consistent with the dihedral calculations, but displaced to greater values [see Fig. 7(e)]. This displacement is caused by the greater-than-expected VV backscatter discussed in Section IV-D.

F. C_{11}/C_{33} [See Fig. 7(f)]

Our observational and theoretical investigations have shown that Fresnel physics leads to an expectation of high HH backscatter and low VV backscatter in areas of vegetation emergent from water. This leads us to consider the ratio C_{11}/C_{33}. This is shown in Fig. 7(f). We note that at steep incidence angles, near the Brewster angle, the C_{33} backscatter is low, making the C_{11}/C_{33} ratio high. This measure shows low scatter and low sensitivity to wood surface moisture as described in Section IV-B. The ratio C_{11}/C_{33} appears to be a very good indicator for areas of inundated vegetation, particularly at steep incidence because of the Brewster angle effect.

G. Cross-Polarized Backscatter [See Fig. 7(g) and (h)]

Now we turn our attention to the cross-pol backscatter, C_{22}. Fig. 7(g) shows the intensity of cross-polarized backscatter, C_{22}, while in Fig. 7(h), we see $C_{22}/(C_{11} + C_{22} + C_{33})$, the ratio of cross-polarized backscatter to total power. We see that the cross-pol backscatter is typically higher for wet conditions, but independent of incidence angle. As a fraction of total power, the cross-pol component increases from about 6% at steep incidence to about 12% at the shallower end of the range, but there is minimal separation of the points obtained under wet conditions. No cross-pol backscatter is predicted with our dihedral model, so there are no theoretical curves shown in Fig. 7(g) and (h). The observed presence of cross-pol backscatter suggests the presence of additional, valuable, information to be found in the data. In the Corrigan swamp, there are numerous upper branches and some curved and nonvertical trunks that may contribute to cross-polarized backscatter, but this possibility must be confirmed through modeling efforts.

V. Conclusion

1) We have provided convincing observational and theoretical evidence that double-bounce backscatter can be misidentified as single-bounce backscatter because of the low CPD that results from the physics of double-bounce reflection from dielectric surfaces with low moisture content.
2) Therefore, we recommend caution when using currently available double-bounce classifications from decomposition models as an indicator of standing water under woody vegetation.
3) Calculations from our simple dihedral model indicate that the CPD should act as a good indicator of wood moisture,

but our observations do not support that hypothesis. Additional modeling work is required to elucidate the physics and develop applications that provide measures of wood moisture.

4) This paper supports the use of steep incidence angles to detect the presence of water under vegetation. The indicators of standing water will be a strong HH return compared to noninundated vegetation, and a high HH/VV ratio.

VI. Next Steps

We need to build upon these results to explore new applications for swamps, marshes, and possibly upland forests. This effort should include the following.

1) Modeling with cylinders over a water, and subsequently soil, substrate.
2) Including nonvertical cylinders to simulate leaning trunks, and branches.
3) Modeling the effects of slightly and moderately rough surfaces for the cylinders and the dielectric substrate.
4) Continuing RADARSAT-2 observations to provide validation and increased understanding of our modeling results.
5) Provide guidance for data acquisition and processing strategies based on research findings.

We encourage other researchers to take note of the importance of accurate modeling of the backscatter physics of targets of interest, in order to maximize the variety and accuracy of applications of the ever-growing availability of polarimetric SAR data.

Acknowledgment

The authors would like to thank the Canadian Space Agency for its valuable Advanced SAR forum for the exchange of ideas. The authors would also like to thank the input and encouragement of Laetitia Thirion-Lefevre of SONDRA/SUPELEC, Paris, France, and the careful review and valuable suggestions of Dr. N. Morandeira of Universidad Nacional de San Martín, Buenos Aires, Argentina. Three anonymous reviewers have contributed significantly to the clarity and completeness of the final manuscript.

References

[1] B. Brisco, F. Ahern, K. Murnaghan, L. White, F. Canisius, and P. Lancaster, "Seasonal change in wetland coherence as an aid to wetland monitoring," *Remote Sens.*, vol. 9, no. 158, pp. 19, Feb. 2017.

[2] B. Brisco *et al.*, "Polarimetric decompositions of temperate wetlands at C-Band," *IEEE J. Sel. Topics Appl. Earth Observ. Remote Sens.*, vol. 8, no. 7, pp. 3583–3594, Jul. 2015.

[3] J. J. Van Zyl, "Unsupervised classification of scattering behavior using radar polarimetry data," *IEEE Trans. Geosci. Remote Sens.*, vol. 27, no. 1, pp. 36–45, Jan. 1989.

[4] A. Freeman and S. L. Durden, "A three-component scattering model for polarimetric SAR data," *IEEE Trans. Geosci. Remote Sens.*, vol. 36, no. 3, pp. 963–973, May 1998.

[5] Y. Yamaguchi, M. Moriama, M. Ishido, and H. Yamada, "Four component scattering model for polarimetric SAR image decomposition," *IEEE Trans. Geosci. Remote Sens.*, vol. 43, no. 8, pp. 1699–1706, Aug. 2005.

[6] S.-H. Hong and S. Wdowinski, "Double bounce component in crosspolarimetric SAR from a new scattering target decomposition," *IEEE Trans. Geosci. Remote Sens.*, vol. 52, no. 6, pp. 3039–3051, Jun. 2014.

[7] F. Ulaby, D. Held, M. C. Dobson, K. C. McDonald, and T. B. A. Senior, "Relating polarization phase difference of SAR signals to scene properties," *IEEE Trans. Geosci. Remote Sens.*, vol. 25, no. 1, pp. 83–92, Jan. 1987.

[8] A. Freeman, "Fitting a two-component scattering model to polarimetric SAR data from forests," *IEEE Trans. Geosci. Remote Sens.*, vol. 45, no. 8, pp. 2583–2592, Aug. 2007.

[9] T. Watanabe, H. Yamada, M. Arii, R. Sato, S.-E. Park, and Y. Yamaguchi, "Experimental study on effects of forest moisture on polarimetric radar backscatter," Presented at the Int. Geosci. Remote Sens. Symp., Quebec, QC, Canada, 2014.

[10] L. Thirion-Lefevre and R. Guinvarc'h, "The double Brewster angle effect," *Comptes Rendus Physique*, vol. 19, no. 1/2, pp. 43–53, Feb. 2018.

[11] Y.-C. Lin and K. Sarabandi, "Electromagnetic scattering model for a tree trunk above a tilted ground plane," *IEEE Trans. Geosci. Remote Sens.*, vol. 33, no. 4, pp. 1063–1070, Jul. 1995.

[12] J. M. López-Sanchez, H. Esteban-González, M. Baquero-Escudero, and J. Fortuny-Guasch, "An electromagnetic scattering model for multiple tree trunks above a tilted rough ground plane," *IEEE Trans. Geosci. Remote Sens.*, vol. 37, no. 2, pp. 659–667, Mar. 1999.

[13] A. Bouvet, T. Le Toan, and N. Lam-Dao, "Monitoring of the rice cropping system in the Mekong delta using ENVISAT/ASAR dual polarization data," *IEEE Trans. Geosci. Remote Sens.*, vol. 47, no. 2, pp. 517–526, Feb. 2009.

[14] J. M. López-Sanchez, "Rice phenology monitoring by means of SAR polarimetry at X-Band," *IEEE Trans. Geosci. Remote Sens.*, vol. 50, no. 7, pp. 2695–2709, Jul. 2012.

[15] J. M. López-Sanchez, F. Vincente-Guijalba, J. D. Ballester-Berman, and S. R. Cloude, "Influence of incidence angle on the coherent copolar polarimetric response of rice at X-Band," *IEEE Trans. Geosci. Remote Sens.*, vol. 12, no. 2, pp. 249–253, Feb. 2015.

[16] S. Cloude, *Polarisation Applications in Remote Sensing*. London, U.K.: Oxford Univ. Press, 2010.

[17] J. A. Richards, *Remote Sensing With Imaging Radar*. New York, NY, USA: Springer, 2009.

[18] F. A. Jenkins and H. E. White, *Fundamentals of Optics*, 3rd ed. New York, NY, USA McGraw-Hill, 1957.

[19] J. D. Jackson, *Electrodynamics*. New York, NY, USA: Wiley, 1962.

[20] M. Born and E. Wolf, *Principles of Optics*, 4th ed. Amsterdam, The Netherlands: Elsevier, 1970.

[21] F. Ulaby and M. El-Rayes, "Microwave dielectric spectrum of vegetation-Part II: Dual-dispersion model," *IEEE Trans. Geosci. Remote Sens.*, vol. GE-25, no. 5, pp. 550–557, Sep. 1987.

[22] L. L. Hess, J. M. Melack, and D. S. Simonett, "Radar detection of flooding beneath the forest canopy: a review," *Int. J. Remote Sens.*, vol. 11, no. 7, pp. 1313–1325, 1990.

[23] F. M. Henderson and A. J. Lewis, "Radar detection of wetland ecosystems: a review," *Int. J. Remote Sens.*, vol. 29, no. 20, pp. 5809–5835, 2008.

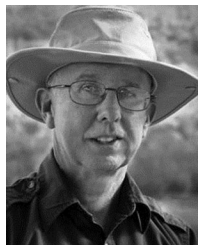

Frank Ahern received the A.B. degree in physics and mathematics from Cornell University, Ithaca, NY, USA, in 1966, and the Ph.D. degree in astrophysics from the University of Maryland, College Park, MD, USA, in 1972.

After two years as a National Science and Engineering Research Council Fellow with the University of Toronto from 1972 to 1974, he joined the Canada Centre for Remote Sensing (CCRS), Ottawa, ON, Canada, as a Research Scientist in 1975, where he remained until 2000. His research activities included radiometric corrections of Landsat data, optical spectrometry, atmospheric corrections, and development of applications of remote sensing data for rangeland and forestry. In 2000, he left CCRS and founded TerreVista Earth Imaging, Brockville, ON, Canada, which has provided remote sensing research services to clients in Canada, the United States, and Europe. He has authored or coauthored 57 articles in refereed journals, 5 books (as author, editor, or chapter author), and more than 125 additional publications.

Dr. Ahern is a member and of the Canadian Remote Sensing Society and was the Editor-in-Chief for the *Canadian Journal of Remote Sensing* from 1985 to 1990. He was the recipient of the Gold Medal of the Canadian Remote Sensing Society for 1991.

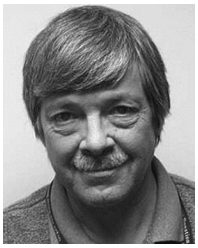

Brian Brisco received the B.Sc. degree in ecology and the M.Sc. degree in soil science from the University of Guelph, Guelph, ON, Canada, in 1977 and 1980, respectively, and the Ph.D. degree in remote sensing/physical geography from the University of Kansas, Lawrence, KS, USA, in 1985.

Since 1975, he has been involved in remote sensing and participated in the SURSAT project from 1977 to 1980. He was a National Science and Engineering Research Council Fellow with the Canada Centre for Remote Sensing (CCRS), Ottawa, ON, Canada, from 1986 to 1989, with Intera Remote Sensing from 1989 to 1997, and with Noetix Research, Inc., Ottawa, ON, Canada, from 1997 to 2004, where he was the Director of Research and Applications Development. In 2004, he joined CCRS as a Research Scientist. He has authored or coauthored more than 200 publications including more than 50 peer reviewed journal publications and is the author of two chapters in the Manual of *Remote Sensing* volume on radar applications published by American Society of Photogrammetry and Remote Sensing. His extensive publications include studies on vegetation characterization, crop identification and monitoring, conservation farming/soil erosion mapping, soil moisture estimation, land cover mapping, wetland mapping, rangeland management, forestry, and developing tools and techniques for ground truth data acquisition. His research interests include interferometry, polarimetry, and radar backscatter modeling including software development and operational implementation, and remote sensing, particularly synthetic aperture radar, for mapping and managing renewable resources.

Dr. Brisco is a member and the Past President of the Canadian Remote Sensing Society.

Kevin Murnaghan received the B.Sc. (Hons.) in applied physics with a minor in computer science from Waterloo University, Waterloo, ON, Canada, in 1996.

Since 2017, he has been with the Canada Centre for Remote Sensing, Ottawa, ON, Canada.

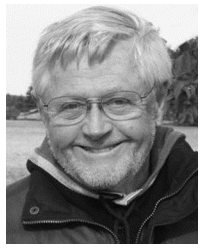

Philip Lancaster received the B.Sc. degree in science geography from McGill University, Montreal, QC, Canada, in 1975.

During his studies, he spent seven years travelling extensively and working at various jobs, including one year at Imperial Chemical Industries of Australia and New Zealand, Botany, NSW, Australia. After graduation, he was with the Pulp and Paper Research Institute of Canada, Pointe-Claire, QC, Canada, and coauthored several papers on the Mechanical Properties of Single Wood Pulp Fibres. After 1980, he was with John Abbott College CEGEP, Ste Anne de Bellevue, QC, Canada, where he developed a new-concept, three-year professional program in energy engineering technology. He retired in 2004 to pursue several personal interests.

Donald K. Atwood (M'95) received the Ph.D. degree in physics from the Massachusetts Institute of Technology (MIT), Cambridge, MA, USA, in 1982.

He was with the AT&T Bell Laboratories and Raytheon's Research Division, where he worked in the field of microlithography. In 1992, he joined MIT Sea Grant, where he developed autonomous underwater vehicles with specialization in underwater acoustics. Then, he worked for Raytheon, first as a Technical Advisor for international environmental programs, then as a Manager in atmospheric remote sensing with the Goddard Space Flight Center. In 2000, he became the Director of the Science Support for the U.S. Antarctic Program. Then, he was the Chief Scientist with the Alaska Satellite Facility, University of Alaska Fairbanks, University of Alaska Fairbanks, Fairbanks, AK, USA, where he focused on applications of SAR, PolSAR, and interferometry for Earth Science. He was a Senior Research Scientist with Michigan Tech Research Institute, where he worked on defense and environmental programs until his retirement in 2016.

Dr. Atwood is a member of the American Geophysical Union and the American Society of Photogrammetry and Remote Sensing.